J. Fluid Mech. (2025), *vol.* 1019, A31, doi:10.1017/jfm.2025.10609

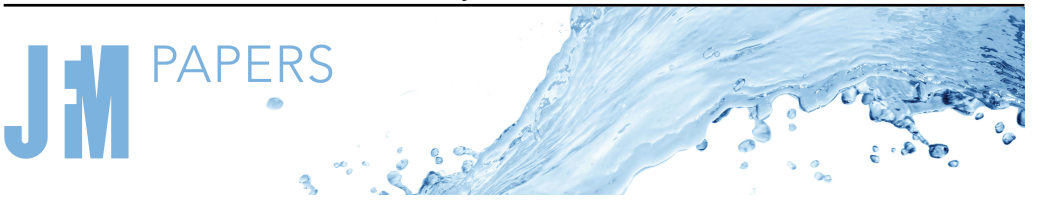

The macroscopic contact angle of water on ice

Wladimir Sarlin[1], **Daniel Vito Papa**[1], **Rodolphe Grivet**[1], **Alexander Rosenbaum**[1], **Axel Huerre**[2], **Thomas Séon**[3] **and Christophe Josserand**[1]

[1]Laboratoire d'Hydrodynamique, CNRS, École polytechnique, Institut Polytechnique de Paris, Palaiseau 91120, France

[2]Laboratoire Matière et Systèmes Complexes (MSC), CNRS, UMR 7057, Université Paris Cité, Paris 75013, France

[3]Institut Franco-Argentin de Dynamique des Fluides pour l'Environnement (IFADyFE), CNRS (IRL 2027), Universidad de Buenos Aires, CONICET, Buenos Aires 1428, Argentina

Corresponding author: Wladimir Sarlin, wladimirsarlin@outlook.com

(Received 3 May 2025; revised 9 August 2025; accepted 17 August 2025)

Wettability quantifies the affinity of a liquid over a substrate and determines whether the surface is repellent or not. When both the liquid and the solid phases are made of the same chemical substance and are at thermal equilibrium, complete wetting is expected in principle, as observed, for instance, with drops of molten metals spreading on their solid counterparts. However, this is not the case for water on ice. Although there is a growing consensus on the partial wetting of water on ice and several estimates available for the value of the associated macroscopic contact angle, the question of whether these values correspond to the contact angle at mechanical and thermal equilibrium is still open. In the present paper, we address this issue experimentally and demonstrate the existence of such a macroscopic contact angle of water on ice, from measurements and theoretical arguments. Indeed, when depositing water droplets on smooth polycrystalline ice layers with accurately controlled surface temperatures, we observe that spreading is unaffected by thermal effects and phase change close enough to the melting point (namely, for undercoolings below 1 K) so that conditions of thermal equilibrium are closely approached. Whereas the short time motion of the contact line is driven by an inertial-capillary balance, the evolution towards mechanical equilibrium is described by a viscous-capillary dynamics and is therefore capillary – and not thermally – related. Moreover, we show that the resulting contact angle remains constant for undercoolings below 1 K. In this way, we show the existence of a non-zero macroscopic contact angle of water on ice under conditions of mechanical and thermal equilibrium, which is very close to 12°. We anticipate this key finding will significantly improve the understanding of capillary flows in the presence of phase change, which is of special interest in the realm of

ice morphogenesis and glaciology, and will also be beneficial with the aim of developing numerical methods for resolving triple-line dynamics.

Key words: drops, wetting and wicking, solidification/melting

1. Introduction

Wetting refers to the science of how a liquid deposited on a solid (or liquid) substrate spreads out. It plays an important role in many aspects of our everyday life such as the first breath of a newborn, underground flows, painting, chemistry, automobile, food industry, three-dimensional (3-D) printing, sap flow in plants or even eye lubrication (de Gennes 1985; Bonn *et al.* 2009). A case of particular interest is that of the wetting of water on its own solid phase, ice. Indeed, a wide variety of ice structures are formed by the freezing of capillary flows (such as drops, rivulets and liquid films), including ice accretion on aeroplanes (Lynch & Khodadoust 2001), power lines (Laforte, Allaire & Laflamme 1998), bridge cables (Liu *et al.* 2019) or wind turbines (Wang 2017); ice falls (Montagnat *et al.* 2010); icicles (Chen & Morris 2011; Papa, Josserand & Cohen 2025); cloud physics (Dash, Rempel & Wettlaufer 2006); frost heave (Wettlaufer & Worster 2006); frozen rivers (Beltaos 2013); and aufeis (Schohl & Ettema 1990). However, despite this ubiquitous coexistence of ice and capillary flows, the wetting behaviour of water on ice remains largely unknown.

From a fundamental point of view, a crystal-clear investigation of the wetting properties of water on ice would require being at thermodynamical equilibrium. With that purpose, an important area of experimental development has been devoted to the characterisation of the shape of a water-like layer at the ice surface at small scales, particularly in the last decades (Sazaki *et al.* 2012; Asakawa *et al.* 2016; Slater & Michaelides 2019). Notably, these authors reported that as ice premelts, a wetting quasi-liquid layer forms on the ice and thickens up to a nanometric thickness that depends on temperature (Murata *et al.* 2016), before the film free surface gets attracted by the ice. This leads to the so-called pseudopartial wetting situation (Brochard-Wyart *et al.* 1991), where the quasi-liquid dewets and forms micrometric water droplets that stand on the film. At such a small scale, the contact angle of micrometric quasi-liquid water droplets has been measured to range between 0.6° and 2.3° (Murata *et al.* 2016), while a recent theoretical analysis predicted a value of 3.4° (Luengo-Márquez *et al.* 2022).

In contrast, at a macroscopic scale, there is a much larger discrepancy in the reported values for the water–ice contact angle (Huerre, Josserand & Séon 2025). These configurations correspond to thicker water layers (typically of the order of the capillary length, i.e. few millimetres) and involve air as the ambient gas. As a result, even if most of these studies attempted to measure a contact angle close to the melting temperature, they are far from the thermodynamic equilibrium. Nevertheless, it should be emphasised that these conditions describe most practical situations where water and ice interact; therefore, characterising the wetting properties of water on ice at mechanical and thermal equilibrium, with air as the ambient gas, is crucial. The first attempt to measure this angle was proposed 60 years ago by Knight (1967), who deposited a puddle of hot water on a cold copper substrate and measured a receding contact angle of 12° at a temperature slightly below 0 °C. A few years later, the same author reported other measurements in various configurations (Knight 1971) and found different values, before ultimately concluding that measuring this angle unequivocally may be impossible, although he thought that the complete wetting scenario is very unlikely (Knight 1996). Since this seminal work,

other authors conducted similar experiments, depositing either a water drop or film on ice and measuring the advancing or receding contact angle, and found values spanning a large range from 6° up to 40° (Makkonen 1997; Thiévenaz *et al.* 2020; Demmenie *et al.* 2023; Grivet *et al.* 2024). In a very recent study, Demmenie *et al.* (2025) performed droplet deposition experiments involving water and ice with varying surface temperature. These authors showed how the apparent angle varies with temperature and also identified 12° as a possible value for the contact angle of water on ice. However, these contributions did not approach the melting point accurately enough, since reaching such a limit remains an experimental challenge, and thereby could not demonstrate that the macroscopic angle they report is observed in the absence of thermal or phase change effects.

Finally, the contact angle θ_e that a water drop makes with ice can be expressed as a function of the three surface energies γ_{iw}, γ and γ_{iv} associated with the solid–liquid, liquid–vapour and solid–vapour interfaces, respectively, using the Young–Dupré relation,

$$\gamma_{iv} = \gamma_{iw} + \gamma \cos\theta_e. \tag{1.1}$$

From then on, a possible path to determine the contact angle of water on ice at thermodynamic equilibrium would be to deduce this angle by considering (1.1). Indeed, given that the surface tension of water at 0 °C is $\gamma = 75.6$ mJ m^{-2} (Lide 2004), θ_e could in theory be estimated using relation (1.1), if both γ_{iv} and γ_{iw} are available. Furthermore, as the Young–Dupré relation remains valid out of thermodynamical equilibrium, provided that effective surface energies are used, this approach could also be used when investigating water–ice–air systems at mechanical and thermal equilibrium. Unfortunately, these values are not known precisely enough today to discriminate between 0° and 50°, as γ_{iw} is currently found to be in the range 27–35 mJ m^{-2} (Espinosa, Vega & Sanz 2016; Ambler *et al.* 2017) and γ_{iv} in the range 70–120 mJ m^{-2} (de Reuck 1957; Ketcham & Hobbs 1969; Van Oss *et al.* 1992; Pruppacher & Klett 2004; Djikaev & Ruckenstein 2017) at 0 °C.

The goal of the present study is thus to characterise the contact angle, if it exists, of water on ice in the thermal equilibrium limit for macroscopic liquid layers. For that purpose, we perform experiments in which a water droplet is deposited on a smooth polycrystalline ice layer whose surface temperature is meticulously varied, to approach thermal equilibrium (i.e. temperature equilibrium between solid and liquid phases) as closely as possible. For temperatures near the melting point, i.e. for undercoolings below 1 K, we demonstrate that the spreading and arrest of the contact line occur independently of thermal effects and phase change. This allows us to report a so-called macroscopic contact angle of water on ice that is robust, non-zero, and observed under conditions of mechanical and thermal equilibrium. Furthermore, for larger undercoolings, we also characterise the evolution of an apparent contact angle of water on ice with temperatures far from thermal equilibrium.

2. Experimental set-up and qualitative results

A schematic of the experimental set-up is illustrated in figure 1(*a*). Experiments consist in depositing a pendent drop of pure demineralised water of density ρ, viscosity η and surface tension γ at vanishing impact velocity (using a linear stage) on a flat layer of ice made of the same pure demineralised water, whose surface temperature is T_i. The spreading of the droplet is recorded with a Photron FASTCAM SA-X2 high-speed camera operating between 8000 and 12 500 frames per second. Both drop and air temperatures (T_d and T_a, respectively) are controlled and kept as close as possible to the melting temperature of water, $T_f = 273.15$ K. Experiments are carried out in a reduced relative

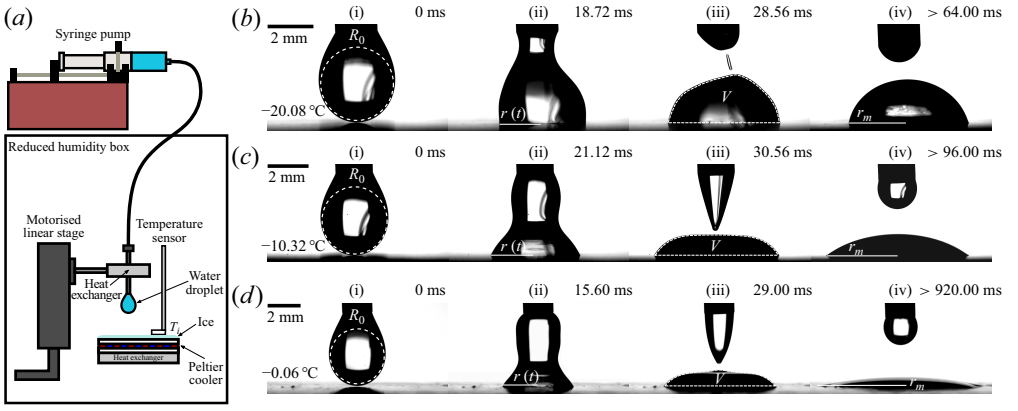

Figure 1. (*a*) Schematics of the experimental set-up. (*b*) Image sequence of the spreading of a water droplet on ice at a low surface temperature ($T_i = -20.08\,^{\circ}\mathrm{C}$). Four representative stages are displayed: (i) just before the initial contact with the ice surface ($t = 0$ ms); (ii) at short time ($t = 18.72$ ms); (iii) when the drop detaches from the needle ($t = 29.76$ ms) and (iv) when motion stops but before complete freezing ($t > 64.00$ ms). (*c*,*d*) Spreading of a droplet on ice at (*c*) a moderately low surface temperature ($T_i = -10.32\,^{\circ}\mathrm{C}$) and (*d*) close to the melting point of water ($T_i = -0.06\,^{\circ}\mathrm{C}$). The same four stages (i)–(iv) are depicted. The initial radius of curvature R_0 of the pendent drop, the radius $r(t)$ of the wetted area, the drop volume V and the arrest radius r_m are highlighted in white.

humidity environment ($RH_a \simeq 16 \pm 2\,\%$) to limit the effect of this parameter on the ice and frost formation (Sebilleau *et al.* 2021). Each test is performed at a constant T_i and repeated five times to ensure reproducibility of the results. In the present study, T_i is varied from close to the melting point up to far out of T_f, i.e. $T_i \in [-0.03\,^{\circ}\mathrm{C}, -20.42\,^{\circ}\mathrm{C}]$, while all other parameters (T_d, T_a, RH_a) are kept constant.

The ice surface is formed by freezing a small layer of water of thickness $\sim$5 mm with a 40×40 mm Peltier cooler mounted on a heat exchanger and connected to a recirculating thermal bath that operates at $T_{bath} = 1 \pm 0.1\,^{\circ}\mathrm{C}$. The thermal bath ensures a proper heat evacuation from the Peltier cooler and therefore a precise control of the thermal flux applied when imposing a voltage. A smooth and mirror-like surface of polycrystalline ice is obtained by enforcing a low thermal flux on the Peltier modulus, typically of the order of $0.1\,\mathrm{K\,min^{-1}}$, which leads to a slow and controlled growth of the solidification front from below. The surface temperature of the ice layer, T_i, is measured by placing a class A flat PT100 RTD sensor (precision of $0.01\,^{\circ}\mathrm{C}$) on top of the ice surface and very close to the deposition site of the droplet (see figure 1*a*). The thermal flux is then gently adapted to set the desired ice temperature T_i. The temperature of the drop, T_d, is controlled by passing the needle (at the tip of which the pendent drop is formed) through a heat exchanger also connected to the recirculating bath. Here, T_d is monitored with a type K thermoelectrical sensor located inside the tip of the needle. Throughout the study, its value was kept at $T_d = 2.5 \pm 0.3\,^{\circ}\mathrm{C}$. The ambient gas temperature T_a is controlled by injecting cold gaseous nitrogen in the box and is measured close to the deposition site with a type K thermoelectric sensor. This parameter is roughly kept constant at $T_a = 7 \pm 1.5\,^{\circ}\mathrm{C}$. The same cold nitrogen influx allows us to set the value of RH_a, which is controlled using a domestic humidity sensor. With such a small value for the reduced relative humidity, we obtained an ice surface that is almost completely dry, in addition to being very smooth. The values of T_a and T_d have been chosen so as to be as close as possible to T_f. Based on preliminary tests, lower droplet temperatures could lead to the partial freezing of the bottom part of

the pendent drop before the initial contact with the ice, while a lower nitrogen temperature would have required an additional cooling system and would have also lowered T_d.

The video recordings are used to monitor the spreading dynamics and to determine all the variables of interest. The initial radius of curvature R_0 of the pendent drop and the water–air surface tension γ are obtained from the last image preceding the onset of spreading (column (i) in figure 1*b–d*) using the pendent drop method introduced by Daerr & Mogne (2016). The radius $r(t)$ of the wetted area is extracted from the contour of the spreading droplets (column (ii) in figure 1*b–d*). The volume V of the drop is computed from the first image following the droplet's detachment from the tip of the needle, when the contrast in the images is at its maximum (column (iii) in figure 1*c–d*). For cold ice surfaces whose undercooling $\Delta T = T_f - T_i > 11$ K, the drop does not detach from the needle axisymmetrically, and hence, V is not computed for these tests. At the end of the spreading process, an extra image is taken (column (iv) in figure 1*b–d*) to compute the arrest radius r_m of the drop and the apparent contact angle θ_a that the droplet forms with the ice. Here, θ_a is determined using an adapted version of the algorithm introduced by Quetzeri-Santiago, Castrejón-Pita & Castrejón-Pita (2020). Furthermore, the density and viscosity of water are taken as $\rho = 1000\ \mathrm{kg\,m^{-3}}$ and $\eta = 1.8 \times 10^{-3}$ Pa s, respectively.

The spreading of the droplet is illustrated in figure 1 for three different surface temperatures $T_i = -20.08\,^{\circ}\mathrm{C}$, $T_i = -10.32\,^{\circ}\mathrm{C}$ and $T_i = -0.06\,^{\circ}\mathrm{C}$ (panels *b*, *c* and *d*, respectively) and at four characteristic moments (columns (i)–(iv)). At the beginning of an experiment, (i) a pendent drop of initial radius of curvature R_0 is put into contact with the ice surface on top of which it starts spreading. (ii) The spreading rate is quantified by considering the radius of the wetted area of the drop on the ice surface, $r(t)$. (iii) At some point in the dynamics, a volume V of liquid detaches from the needle. (iv) When spreading ceases, this volume eventually stabilises to form a sessile droplet that exhibits a spherical cap shape of arrest radius r_m. For large undercoolings ΔT, the drop shape is similar to a hemisphere and its apparent contact angle θ_a with the substrate is high (figure 1*b*,iv), whereas for ice surface temperature approaching the melting point of water T_f, the sessile drop resembles a very thin lens with a small but non-zero contact angle (figure 1*d*,iv).

3. Results and discussion

3.1. *Spreading dynamics*

The evolution of the dimensionless radius r/R_0 with the rescaled time t/τ_c is presented in figure 2(*a*) for five representative ice surface temperatures, T_i. Here, $\tau_c = \sqrt{\rho {R_0}^3/\gamma}$ is the inertial-capillary time scale. A first phase of fast spreading is observed for all experiments (before the black arrows), which is reminiscent of the short-time evolution observed for isothermal droplet deposition experiments (Biance, Clanet & Quéré 2004; Bird, Mandre & Stone 2008; Winkels *et al.* 2012). This regime ends at a time t_{ic}, which depends on the ice temperature. For the dark blue curve in figure 2(*a*), corresponding to $T_i = -20.08\,^{\circ}\mathrm{C}$ (•) and to sequence (*b*) in figure 1, a partial-pinning of the contact line is observed from $t/\tau_c \simeq 0.8$ up to $t/\tau_c \simeq 4.1$, when the arrest radius is reached. Such a behaviour causes the asymmetry of the free-surface of the spreading drop in figure 1(*b*,ii) (compared with figures 1*c*,ii or 1*d*,ii). This observation suggests that, for a cold enough ice surface, the contact line can undergo pinning and unpinning due to interactions between the advancing contact line and the ice layer that grows beneath the spreading drop. For moderate ice surface temperatures, a different evolution is noticed, as illustrated by the two curves corresponding to $T_i = -2.92\,^{\circ}\mathrm{C}$ (•) and $T_i = -10.30\,^{\circ}\mathrm{C}$ (•) in figure 2(*a*). Indeed, for these experiments, the fast spreading dynamics abruptly stops

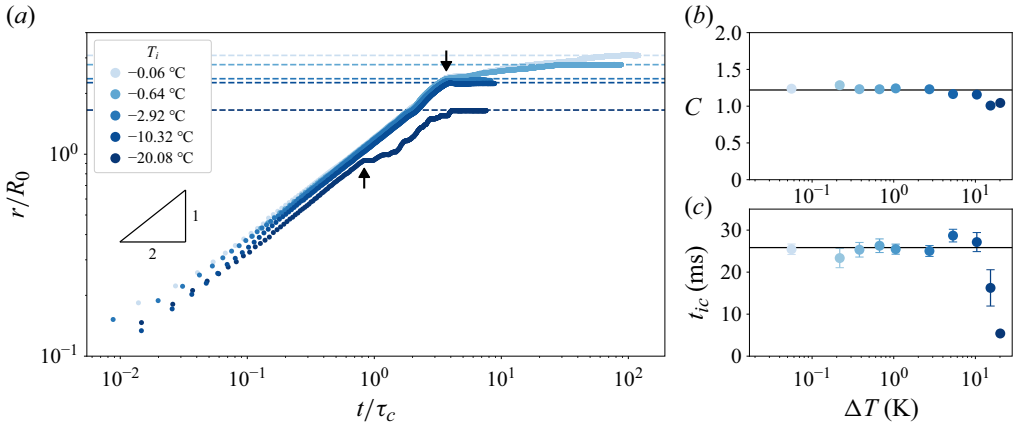

Figure 2. (*a*) Dimensionless spreading radius, r/R_0, as a function of the rescaled time, t/τ_c, in a logarithmic scale. The horizontal dashed lines highlight the arrest radius reached for each experiment. (*b*) Evolution of the numerical prefactor C from (3.1) with the undercooling $\Delta T = T_f - T_i$, with T_f the melting point of water. The solid line represents $C = 1.22$. (*c*) t_{ic} as a function of ΔT. The solid line indicates $t_{ic} = 25.84$ ms. The colours of the symbols denote the surface temperature T_i of the ice, with darker shades corresponding to colder ice.

around $t/\tau_c \simeq 3.8$ without any significant partial-pinning of the contact line afterwards. Finally, for ice surface temperatures closer to the melting point, a second and slower dynamics takes place after the sudden stop of the initial fast spreading regime. This is illustrated by the light blue curves in figure 2(*a*), corresponding to $T_i = -0.06\,°\mathrm{C}$ (●) and to $T_i = -0.64\,°\mathrm{C}$ (●), from $t/\tau_c \simeq 3.8$ onward. For all experiments, the horizontal dashed line whose colour corresponds to the symbols indicates the arrest radius r_m reached at the end of the spreading process.

The short-time dynamics is well described by a balance between Laplace pressure, which drives the motion, and the inertial pressure that resists it (Biance *et al.* 2004; Bird *et al.* 2008; Winkels *et al.* 2012; Grivet *et al.* 2022). Indeed, equating the two effects gives the following inertial-capillary dynamics for the radius of the wetted area

$$\frac{r(t)}{R_0} = C\left(\frac{t}{\tau_c}\right)^{1/2}, \tag{3.1}$$

with C a numerical prefactor. It can be observed in figure 2(*a*) that the short-time evolution of the dimensionless radius, before each of the black arrows, effectively displays a square root of time evolution, as evidenced by the 1/2 slope followed by all curves in this first dynamical regime. It has been verified that this $1/2$ power law is insensitive to errors in determining the time origin, given the large temporal resolution at which the experiments were recorded. The prefactor C is systematically extracted and presented in figure 2(*b*) as a function of the undercooling $\Delta T = T_f - T_i$. For $\Delta T < 11$ K, C plateaus at a constant value of 1.22, which is consistent with the measurements reported by Bird *et al.* (2008) ($C \in [0.75, 1.5]$) and Grivet *et al.* (2022) ($C = 1.15 \pm 0.06$) for droplet deposition experiments. For undercoolings beyond 11 K, a slight decrease of C is noticed, which can be attributed to the increasing rate of solidification. Strikingly, the constant value of C over two decades of ΔT between 0.06 and 11 K reveals that this inertial-capillary regime is unaffected by the ice surface temperature. In other words, the contact line dynamics of the spreading droplet in this regime is insensitive to both temperature gradients and phase change at short times. The arrest time of this inertial-capillary dynamics, t_{ic}, is then determined for all experiments. Its evolution with undercooling ΔT is illustrated

in figure 2(*c*), where it can be seen that t_{ic} remains constant at approximately 25.84 ms when $\Delta T < 11$ K, before dropping sharply for higher undercooling. This demonstrates that, for $\Delta T > 11$ K, solidification does induce an early pinning of the advancing contact line during the inertial-capillary regime, whereas for smaller undercooling, the arrest of this dynamics is not thermally related.

Then, two different situations are observed when $\Delta T < 11$ K. In the intermediate range $1\ \text{K} < \Delta T < 11$ K, the spreading of the droplet ceases right after the inertial-capillary regime, as highlighted by the experiments at $T_i = -2.92\,^{\circ}\text{C}$ (•) and $T_i = -10.3\,^{\circ}\text{C}$ (•) in figure 2(*a*), where no motion occurs after t_{ic}. However, a second and slower dynamics systematically takes place when $\Delta T < 1$ K, as illustrated by experiments where $T_i = -0.06\,^{\circ}\text{C}$ (•) and $T_i = -0.64\,^{\circ}\text{C}$ in figure 2(*a*). We suspect this second regime to correspond to a viscous-capillary spreading. Indeed, in the absence of thermal effects, such dynamics usually develops once inertia becomes negligible (Biance *et al.* 2004; Bonn *et al.* 2009). As discussed in particular by De Gennes (1984), this behaviour is intimately related to wettability that governs the manner the contact line relaxes to equilibrium. In the case of total wetting, one would expect Tanner's law to be valid, so that $r/R_v \propto (\gamma t/(\eta R_v))^{1/10}$, with $R_v = (3V/(4\pi))^{1/3}$ the equivalent radius for a droplet of initial volume V (Tanner 1979; De Gennes 1984). However, if partial wetting is at play, a viscous-capillary spreading (similar to a Cox–Voinov dynamics) is expected for the moving contact line (Voinov 1976; de Gennes 1985; Cox 1986; Bonn *et al.* 2009). To describe the motion of the contact line for a spreading droplet of initial volume V and equivalent radius $R_v = (3V/(4\pi))^{1/3}$, we consider the following set of equations:

$$\frac{\mathrm{d}\tilde{r}}{\mathrm{d}\tilde{t}} = \frac{1}{3\zeta}\tan\theta(\tilde{t})(\cos\theta_e - \cos\theta(\tilde{t})), \tag{3.2}$$

$$\frac{\tilde{r}^3}{4\sin^3\theta(\tilde{t})}(2 + \cos^3\theta(\tilde{t}) - 3\cos\theta(\tilde{t})) = 1, \tag{3.3}$$

where $\tilde{t} = t/\tau_v$, $\tilde{r} = r/R_v$ and $\tau_v = \eta R_v/\gamma$ the viscous-capillary time scale, and where $\theta(\tilde{t})$ and θ_e are the instantaneous and equilibrium macroscopic contact angles, respectively. Equation (3.2) is obtained by balancing viscous dissipation at the contact line with the action of capillary forces that drive the motion (see Appendix A for details on the derivation), whereas (3.3) is the conservation of volume for a spherical cap (Van de Velde *et al.* 2023). In the former relation, ζ is a dimensionless parameter related to the ratio between the typical length scale of the system (e.g. the droplet radius R_v) and a microscopic length of the order of a nanometre; it enables matching between the microscopic and macroscopic solutions describing the shape of the contact line (Bonn *et al.* 2009). Since all the present experiments involve water droplets with a rather constant initial radius that are deposited on the same substrate (ice), ζ can reasonably be considered constant. From then on, (3.2)–(3.3) can straightforwardly be solved numerically, with θ_e being evaluated from (3.3) when $r = r_m$ and $\theta = \theta_e$ (thus, θ_e is the macroscopic contact angle that the drop reaches at the end of spreading).

The evolution of $\tilde{r}$ with $\tilde{t}$ is illustrated in figure 3(*a*) for two experiments where $T_i = -0.06\,^{\circ}\text{C}$ (•) and $T_i = -0.64\,^{\circ}\text{C}$ (•). The two curves highlight the relaxation of the wetted radius up to its arrest value r_m, which is reported as horizontal dashed lines. The corresponding predictions from (3.2)–(3.3), with $\zeta = 30$, are also reported as solid black lines in figure 3(*a*). This value for ζ has been obtained by adjusting a theoretical curve to one experiment, and has then been used to describe all tests where $\Delta T < 1$ K. Indeed, although it is based on physical grounds and expected to be constant for the reasons indicated previously, there is no analytical estimate available to determine its

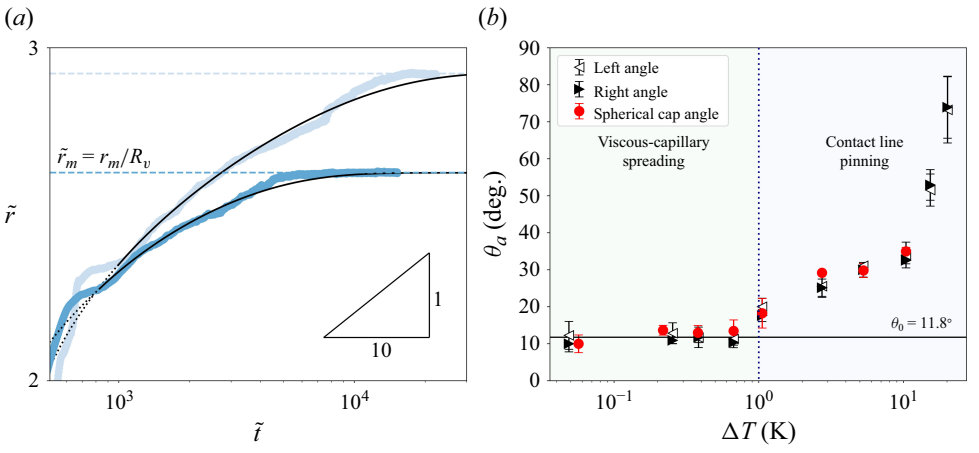

Figure 3. (*a*) Rescaled radius $\tilde{r} = r/R_v$ as a function of $\tilde{t} = t/\tau_v$, in the viscous-capillary regime, for two experiments where $T_i = -0.06\,°\mathrm{C}$ (●) and $T_i = -0.64\,°\mathrm{C}$ (●) (in logarithmic representation). The solid lines are the corresponding predictions obtained by solving (3.2)–(3.3), which are extended as dotted lines prior to the observed viscous-capillary spreading. The 1/10 slope that would correspond to complete wetting (Tanner's law) is also indicated. The horizontal lines highlight the dimensionless arrest radius $\tilde{r}_m = r_m/R_v$ reached for each experiment. (*b*) Evolution of the apparent contact angle θ_a as a function of the undercooling ΔT. The black and white triangles respectively correspond to measurements of the right and left angles between the water droplet and the ice once the final state is reached, using the method described by Quetzeri-Santiago *et al.* (2020). The red circles are the apparent angles estimated using (3.3) with $r = r_m$, i.e. assuming the final shape is a spherical cap. The solid line is the plateau $\theta_0 = 11.8°$, which is the mean contact angle measured from all experiments where $\Delta T < 1$ K.

value. The theoretical solutions closely match the experimental measurements for the two ice surface temperatures, from the onset of the second regime to the stabilisation of the spreading drop. This result reveals that the slower spreading phase observed when $\Delta T < 1$ K is also insensitive to phase change or to any thermal effect. The differences between the two curves, for instance, in terms of the final radius, are not due to the ice temperature (as this parameter is not involved in (3.2)–(3.3)) but only to fluctuations in V or in the thermophysical properties of water that are captured by the present modelling. Furthermore, the dynamics is well described by a viscous-capillary evolution and the two experiments significantly depart from a 1/10 power law during the relaxation of the contact line. This key observation demonstrates that the arrest of the drop is solely due to capillary effects, with no influence from temperature, and that water partially wets ice. In fact, one can easily argue that thermal effects related to solidification vanish towards the capillary ones as the melting point is approached. Indeed, we can estimate the solidification time scale as $\tau_{sol} = h^2/D_{eff}$, where h is the typical thickness of the water film at maximal spreading and D_{eff} is the effective diffusion coefficient of ice growth when water is in contact with it (Sarlin *et al.* 2024). Then, in the small ΔT limit, one has $D_{eff} \propto \Delta T^2$ (see more detail in Appendix B). However, the inertial-capillary and viscous-capillary dynamics are respectively based on the time scales $\tau_c = \sqrt{\rho {R_0}^3/\gamma}$ and $\tau_v = \eta R_v/\gamma$ that are mostly independent of temperature. Therefore, when comparing these two typical times to the solidification time scale, it is clear that in the limit $\Delta T \to 0$, the spreading dynamics becomes unaffected by phase change as thermal equilibrium is approached. In contrast, for large ΔT, solidification will become dominant, which agrees with the observation of the partial-pinning effect observed near the triple line at the lowest

ice surface temperatures investigated (see Appendix B for details about the comparison of the time scales).

Hence, for undercoolings below 1 K, the inertial-capillary dynamics is followed by a viscous-capillary regime that is well described by a model independent of thermal effects and phase change, which strongly suggests that we are closely approaching thermal equilibrium in this range of ice surface temperature.

3.2. *The macroscopic contact angle of water on ice*

To further discuss the value of the macroscopic contact angle of water on ice under the present experimental conditions, the apparent angle θ_a between the droplet and the ice layer at the end of the spreading process is systematically extracted in two different manners. First, the right and left angles are evaluated from the contours of the final photograph taken for each experiment, using the algorithm developed by Quetzeri-Santiago *et al.* (2020) to ensure reliable measurements. By doing so, the contact line is approximated by first- or second-order polynomials, and the most robust tangent at the triple line is retained. Second, an independent estimate is obtained by using (3.3) with the initial volume V and the final measured radius r_m, assuming the final liquid film has a spherical cap shape. This second method is only applied to experiments where $\Delta T < 11$ K, due to the reasons mentioned in § 2. The results are illustrated in figure 3(*b*), where θ_a is presented as a function of the undercooling ΔT. The apparent angle is large when ΔT is greater than 11 K, as the contact line gets pinned during the short-time dynamics where its curvature is important. It then decays when the undercooling is reduced. A first inflection of the curve is observed around $\Delta T \simeq 11$ K, i.e. when contact line pinning occurs at the end of the inertial-capillary regime. Finally, θ_a reaches a constant value θ_0 that is seen over more than a decade when $\Delta T < 1$ K, for both measurement methods. The average value and standard deviation for this constant macroscopic contact angle are

$$\theta_0 = 11.8^\circ \pm 1.2^\circ. \tag{3.4}$$

Interestingly, this estimate is significantly above zero, even including measurement errors from both methods.

Therefore, θ_a is independent of temperature for undercoolings up to approximately 1 K. Beyond this limit, however, temperature begins to play a dominant role and the apparent contact angle increases with ΔT. Based on the observations in figure 3(*b*) and the aforementioned discussion on the spreading dynamics, which is insensitive to thermal effects close enough to the melting point, we conclude that θ_0 is the advancing contact angle of water on ice under conditions of mechanical and thermal equilibrium. Due to the nano-smooth surface state of ice at small undercoolings, contact line hysteresis must be very small in this case (Bonn *et al.* 2009); hence, θ_0 is expected to be very close to the macroscopic equilibrium contact angle. Finally, it is striking to note that the present estimate for the macroscopic angle of water on ice is strongly supported by the results from numerous similar studies (Knight 1967; Thiévenaz *et al.* 2020; Grivet *et al.* 2024; Demmenie *et al.* 2023, 2025), which were performed under different drop and ambient gas temperatures and relative humidity conditions. Owing to this observation, we infer that the the macroscopic contact angle we report is not significantly impacted by humidity and evaporative effects.

4. Conclusion

In the present investigation, droplet deposition experiments are reported that demonstrate the partial wetting of water on ice. Indeed, close enough to the melting point of water,

i.e. when $\Delta T < 1$ K, the spreading dynamics is found to be independent of thermal effects, causing the liquid film to relax into a sessile droplet shape. In this temperature range, a short-time inertial-capillary regime takes place first and is followed by a viscous-capillary dynamics. At the end of the spreading process, a macroscopic advancing contact angle of water on ice very close to 12° is identified. If this value agrees with previous estimates, the key findings here are to show that the slow evolution of the contact line in the second regime corresponds to a viscous-capillary dynamics, which implies that the observed angle is only due to wetting without any thermal effects, and that there is a smooth asymptotic convergence of the contact angle with decreasing undercooling. These two elements put together allow us to assert that for $\Delta T < 1$ K, we reach mechanical and thermal equilibrium. Furthermore, because the ice layer is dry and nano-smooth due to the reduced humidity and slow formation rate, the contact angle hysteresis is expected to be small in this case. Although reducing the relative humidity implies that the present experiments are not performed at vapour pressure equilibrium (i.e. far from thermodynamic equilibrium), our measurements remarkably agree with numerous similar studies that operated under different relative humidity conditions (Knight 1967; Thiévenaz *et al.* 2020; Demmenie *et al.* 2023; Grivet *et al.* 2024; Demmenie *et al.* 2025), thereby suggesting that this parameter does not have a significant influence. Therefore, we infer that the value of the advancing contact angle θ_0 reported here is robust and close to the macroscopic equilibrium contact angle of water on its solid phase.

As mentioned in the introduction of the present work, two main groups of results exist. In the first, a microscopic contact angle around or less than one degree has been reported by thermodynamic studies, whereas in the second, a larger macroscopic contact angle is obtained from fluid mechanics studies (Huerre *et al.* 2025). Although the present results suggest that the macroscopic contact angle of water on ice is very close to 12°, it already appears that there is a clear need to understand the origin of the discrepancy between small- and large-scale observations. Solving this issue is of great interest and definitely deserves further investigations, which might rely on recent experimental techniques such as phase-shifting profilometry (de Miramon *et al.* 2025).

The outcomes of the present study also allow us to provide an estimate of the difference between the ice–air and ice–water surface energies (respectively γ_{ia} and γ_{iw}). For that purpose, one can use the Young–Dupré relation (1.1) to write $\gamma_{ia} - \gamma_{iw} = \gamma \cos\theta_0 \simeq 73.9$ mN m^{-1}, using $\theta_0 = 12°$ and $\gamma = 75.6$ mN m^{-1}. From then on, it can be mentioned that estimates for γ_{iw} available in the literature lie in the small range [27−35] mN m^{-1} (Huerre *et al.* 2025). Using those two extreme values to compute the ice–air surface energy, this suggests that γ_{ia} is between 101 mN m^{-1} and 109 mN m^{-1}. So far, several studies gave different estimates for this parameter, spanning a large range from 70 mN m^{-1} to 120 mN m^{-1} notably due to the lack of consensus on the contact angle of water on ice (Huerre *et al.* 2025). The findings reported here, in particular, the robust measurement of θ_0, thereby allow us to infer a narrower range for γ_{ia}, which goes in the sense of Ketcham & Hobbs (1969) and Pruppacher & Klett (2004).

We anticipate these results to be of significant importance to better understand the formation of ice structures resulting from the interaction between capillary flows and phase change. The knowledge of the contact angle of water on ice in environmental conditions as well as the ice–air surface energy is also expected to be valuable to improve current numerical simulations dealing with three-phase problems at the macroscopic scale. Given the detailed description of the spreading dynamics of a water droplet on ice provided here, this model experiment could constitute a benchmark test for the development of numerical methods. More broadly, the outcomes of the present study bring new insights

on the manner water covers ice, and could thereby be applied to the study of ice melt in glaciology.

Acknowledgments. The authors warmly thank C. Frot and A. Garcia for their help in the elaboration of the experimental set-up.

Funding. This work was supported by Agence de l'Innovation de Défense (AID) – via Centre Interdisciplinaire d'Etudes pour la Défense et la Sécurité (CIEDS) – (project 2021 - ICING).

Competing interests. The authors report no conflict of interest.

Author contributions. W. S. and D. V. P. contributed equally to the present study.

Data availability statement. The data that support the findings of this study are available from the corresponding author, upon reasonable request.

Appendix A. The viscous-capillary spreading

Once the inertial-capillary dynamics ends, a second regime takes place that involves this time a competition between surface tension, which drives the motion, and viscous dissipation. In what follows, we denote by U the velocity of the contact line, r the radius of the wetted area, θ the macroscopic contact angle and u the velocity of the fluid (all these quantities depend on time). We assume that u has a parabolic profile with respect to the vertical direction, so that

$$u(z) = \frac{3}{2}U\left(\frac{2z}{\xi} - \frac{z^2}{\xi^2}\right), \tag{A1}$$

with z the vertical distance from the substrate and $\xi = \alpha \tan\theta$ the position of the free surface, which depends on the horizontal distance α from the triple point. In that situation, the power density is $\eta(\partial u/\partial z)^2$ (Guyon, Hulin & Petit 2012), so that the dissipation per unit length reads

$$D = \int_{\alpha_m}^{\alpha_M}\int_0^{\xi} \eta\left(\frac{\partial u}{\partial z}\right)^2 \mathrm{d}z\,\mathrm{d}\alpha = \frac{3\eta U^2}{\tan\theta}\zeta, \tag{A2}$$

where $\zeta = \ln(\alpha_M/\alpha_m)$ depends on two quantities α_m and α_M (of the order of a nanometre and of the typical size of the system, respectively) and allows one to match the microscopic and macroscopic shapes of the contact line (Bonn *et al.* 2009).

On the other hand, the capillary force per unit length which acts on the contact line can be expressed as $F_c = \gamma_{sg} - \gamma\cos\theta - \gamma_{sl}$, with γ_{sg} and γ_{sl} the surface energies associated with the solid–gas and solid–liquid interfaces, respectively. As F_c vanishes when the equilibrium contact angle θ_e is reached, we also have $\gamma_{sg} = \gamma_{sl} + \gamma\cos\theta_e$. Thus, we have $F_c = \gamma(\cos\theta_e - \cos\theta)$ and the power (per unit length) this force induces is $F_c U$. If it gets fully dissipated, we thereby have

$$\gamma\,(\cos\theta_e - \cos\theta)\,U = \frac{3\eta\zeta}{\tan\theta}U^2, \tag{A3}$$

which can be rewritten, as $U = \mathrm{d}r/\mathrm{d}t$, in the form

$$\frac{\mathrm{d}\tilde{r}}{\mathrm{d}\tilde{t}} = \frac{1}{3\zeta}\tan\theta\,(\cos\theta_e - \cos\theta)\,, \tag{A4}$$

with $\tilde{r} = r/R_v$ and $\tilde{t} = t/\tau_v$ ($R_v = (3V/(4\pi))^{1/3}$ being the equivalent radius based on the initial volume V of liquid deposited, and $\tau_v = \eta R_v/\gamma$ the typical viscous-capillary time scale). Equation (A4) is the same as (3.2) in the main text.

A case of particular interest is the situation of complete wetting, i.e. when $\theta_e = 0$. When this is the case, assuming $\theta \ll 1$, (A4) reduces to

$$\frac{\mathrm{d}r}{\mathrm{d}t} = \frac{\gamma}{6\eta\zeta}\theta^3 \propto \frac{\gamma}{\eta}\theta^3, \tag{A5}$$

as ζ can approximately be considered constant (De Gennes 1984). Then, by observing that, for small angles, we have $\theta \simeq 2e/r$ for a spherical cap of radius r and uppermost height e, and that a rough conservation of volume implies $r^2 e \propto {R_v}^3$, (A5) leads to

$$r^9 \frac{\mathrm{d}r}{\mathrm{d}t} \propto \frac{\gamma}{\eta}{R_v}^9, \tag{A6}$$

which, after integration, gives

$$\frac{r}{R_v} \propto \left(\frac{t}{\tau_v}\right)^{1/10}. \tag{A7}$$

Equation (A7), widely known as Tanner's law, describes the spreading of a viscous drop of a completely wetting liquid (Tanner 1979).

Appendix B. Spreading and solidification time scales

The time needed to solidify a droplet of volume V and radius $R_v = (3V/(4\pi))^{1/3}$ can be estimated via the self-similar solution of the Stefan problem, which gives in particular the evolution of the solidification front $h = \sqrt{D_{eff}\, t}$. In this expression, D_{eff} is an effective diffusion coefficient that is the solution to a transcendental equation involving the thermal properties of the different phases and the undercooling ΔT (Thiévenaz *et al.* 2019; Sarlin *et al.* 2024). Considering that, at maximal spreading r_m, the droplet has a characteristic height $h \propto {R_v}^3/{r_m}^2$, the typical solidification time scale writes

$$\tau_{sol} = \frac{{R_v}^6}{{r_m}^4 D_{eff}}. \tag{B1}$$

Similarly, it is possible to estimate the time scale τ_{ic} needed to reach the maximal spreading diameter in the inertial-capillary regime from the scaling law $r/R_0 \propto (t/\tau_c)^{1/2}$, which yields (here, we take $R_0 \simeq R_v$ for the sake of simplicity)

$$\tau_{ic} = \sqrt{\frac{\rho {R_v}^3}{\gamma}}\left(\frac{r_m}{R_v}\right)^2. \tag{B2}$$

Conversely, the viscous-capillary time scale τ_{vc} is obtained from the scaling $r/R_v \propto (\gamma t/(\eta R_v))^{1/10}$ (see Appendix A), which leads this time to

$$\tau_{vc} = \frac{\eta R_v}{\gamma}\left(\frac{r_m}{R_v}\right)^{10}. \tag{B3}$$

With these three times, it is possible to derive two dimensionless ratios comparing the solidification time scale with the inertial-capillary or viscous-capillary ones. They respectively write

$$\frac{\tau_{sol}}{\tau_{ic}} = \frac{1}{D_{eff}}\sqrt{\frac{\gamma R_v}{\rho}}\left(\frac{R_v}{r_m}\right)^6 \quad \text{and} \quad \frac{\tau_{sol}}{\tau_{vc}} = \frac{1}{D_{eff}}\frac{\gamma R_v}{\eta}\left(\frac{R_v}{r_m}\right)^{14}. \tag{B4}$$

In both cases, one can observe that they are inversely proportional to D_{eff}. Then, for undercoolings approaching 0, one has

$$D_{eff} \sim \frac{4 D_i {c_{p,i}}^2}{\pi {\mathcal{L}_f}^2} \Delta T^2, \tag{B5}$$

with D_i and $c_{p,i}$ the ice thermal diffusivity and heat capacity, and $\mathcal{L}_f$ the latent heat of fusion for water (Thiévenaz *et al.* 2019). As a result, when $\Delta T \to 0$, the ratios of time scales will tend to infinity as fast as ΔT^2. This implies that, close to the melting point, the solidification rate rapidly becomes negligible compared with the spreading dynamics, regardless of the drop size or the maximal spreading radius. However, for large undercoolings, the solidification rate becomes important and causes the partial-pinning effect observed near the triple line.

References

Ambler, M., Vorselaars, B., Allen, M.P. & Quigley, D. 2017 Solid–liquid interfacial free energy of ice ih, ice ic, and ice 0 within a mono-atomic model of water via the capillary wave method. *J. Chem. Phys.* **146** (7), 074701.

Asakawa, H., Sazaki, G., Nagashima, K., Nakatsubo, S. & Furukawa, Y. 2016 Two types of quasi-liquid layers on ice crystals are formed kinetically. *Proc. Natl Acad. Sci. USA* **113** (7), 1749–1753.

Beltaos, S. 2013 *River Ice Formation. Committee On River Ice Processes and the Environment*. Canadian Geophysical Union.

Biance, A.-L., Clanet, C. & Quéré, D. 2004 First steps in the spreading of a liquid droplet. *Phys. Rev. E* **69**, 016301.

Bird, J.C., Mandre, S. & Stone, H.A. 2008 Short-time dynamics of partial wetting. *Phys. Rev. Lett.* **100**, 234501.

Bonn, D., Eggers, J., Indekeu, J., Meunier, J. & Rolley, E. 2009 Wetting and spreading. *Rev. Mod. Phys.* **81**, 739–805.

Brochard-Wyart, F., Di Meglio, J.-M., Quére, D. & De Gennes, P.-G. 1991 Spreading of nonvolatile liquids in a continuum picture. *Langmuir* **7** (2), 335–338.

Chen, A.S.-H. & Morris, S.W. 2011 Experiments on the morphology of icicles. *Phys. Rev. E* **83**, 026307.

Cox, R.G. 1986 The dynamics of the spreading of liquids on a solid surface. Part 1. Viscous flow. *J. Fluid Mech.* **168**, 169–194.

Daerr, A. & Mogne, A. 2016 Pendent_drop: an imagej plugin to measure the surface tension from an image of a pendent drop. *J. Open Res. Softw.* **4** (1), e3.

Dash, J.G., Rempel, A.W. & Wettlaufer, J.S. 2006 The physics of premelted ice and its geophysical consequences. *Rev. Mod. Phys.* **78**, 695–741.

De Gennes, P.-G. 1984 Dynamique d'étalement d'une goutte. *Comptes-rendus des séances de l'Académie des sciences. Série 2, Mécanique-physique, chimie, sciences de l'univers, sciences de la terre* **298** (4), 111–115.

Demmenie, M., Gorin, B., Kolpakov, P., Smith, S., Kellay, H. & Bonn, D. 2025 Partial wetting of water on ice. *Phys. Rev. Fluids* **10**, 054002.

Demmenie, M., Reus, L., Kolpakov, P., Woutersen, S., Bonn, D. & Shahidzadeh, N. 2023 Growth and form of rippled icicles. *Phys. Rev. Appl.* **19**, 024005.

Djikaev, Y.S. & Ruckenstein, E. 2017 Self-consistent determination of the ice–air interfacial tension and ice–water–air line tension from experiments on the freezing of water droplets. *J. Phys. Chem. C* **121** (30), 16432–16439.

Espinosa, J.R., Vega, C. & Sanz, E. 2016 Ice–water interfacial free energy for the TIP4P, TIP4P/2005, TIP4P/Ice, and mW models as obtained from the mold integration technique. *J. Phys. Chem. C* **120** (15), 8068–8075.

de Gennes, P.-G. 1985 Wetting: statics and dynamics. *Rev. Mod. Phys.* **57**, 827–863.

Grivet, R., Huerre, A., Séon, T., Duchemin, L. & Josserand, C. 2024 Freezing receding contact lines. arXiv:2409.00385

Grivet, R., Monier, A., Huerre, A., Josserand, C. & Séon, T. 2022 Contact line catch up by growing ice crystals. *Phys. Rev. Lett.* **128**, 254501.

Guyon, É., Hulin, J.-P. & Petit, L. 2012 *Hydrodynamique Physique 3e édition*. EDP Sciences.

HUERRE, A., JOSSERAND, C. & SÉON, T. 2025 Freezing and capillarity. *Annu. Rev. Fluid Mech.* **57** (2025), 257–284.
KETCHAM, W.M. & HOBBS, P.V. 1969 An experimental determination of the surface energies of ice. *Phil. Mag. J. Theor. Exp. Appl. Phys.* **19** (162), 1161–1173.
KNIGHT, C.A. 1967 The contact angle of water on ice. *J. Colloid Interface Sci.* **25** (2), 280–284.
KNIGHT, C.A. 1971 Experiments on the contact angle of water on ice. *Phil. Mag. J. Theor. Exp. Appl. Phys.* **23** (181), 153–165.
KNIGHT, C.A. 1996 Surface layers on ice. *J. Geophys. Res.: Atmos.* **101** (D8), 12921–12928.
LAFORTE, J.L., ALLAIRE, M.A. & LAFLAMME, J. 1998 State-of-the-art on power line de-icing. *Atmos. Res.* **46** (1), 143–158.
LIDE, D.R. 2004 *CRC Handbook of Chemistry and Physics*, vol. **85**. CRC Press.
LIU, Y., CHEN, W., PENG, Y. & HU, H. 2019 An experimental study on the dynamic ice accretion processes on bridge cables with different surface modifications. *JWEIA* **190**, 218–229.
LUENGO-MÁRQUEZ, J., IZQUIERDO-RUIZ, F. & MACDOWELL, L.G. 2022 Intermolecular forces at ice and water interfaces: premelting, surface freezing, and regelation. *J. Chem. Phys.* **157** (4), 044704.
LYNCH, F.T. & KHODADOUST, A. 2001 Effects of ice accretions on aircraft aerodynamics. *Prog. Aerosp. Sci.* **37** (8), 669–767.
MAKKONEN, L. 1997 Surface melting of ice. *J. Phys. Chem. B* **101** (32), 6196–6200.
DE MIRAMON, H., SARLIN, W., HUERRE, A., COBELLI, P., SÉON, T. & JOSSERAND, C. 2025 Free surface topography of capillary flows using spatiotemporal phase shifting profilometry. *Exp. Fluids* **66** (5), 89.
MONTAGNAT, M., WEISS, J., CINQUIN-LAPIERRE, B., LABORY, P.A., MOREAU, L., DAMILANO, F. & LAVIGNE, D. 2010 Waterfall ice: formation, structure and evolution. *J. Glaciol.* **56** (196), 225–234.
MURATA, K.-I., ASAKAWA, H., NAGASHIMA, K., FURUKAWA, Y. & SAZAKI, G. 2016 Thermodynamic origin of surface melting on ice crystals. *Proc. Natl Acad. Sci. USA* **113** (44), E6741–E6748.
PAPA, D., JOSSERAND, C. & COHEN, C. 2025 Shape of ice stalagmites. *Phys. Rev. Fluids*. Available at: https://journals.aps.org/prfluids/accepted/10.1103/sc66-hrv2.
PRUPPACHER, H.R. & KLETT, J.D. 2004 *Microphysics of Clouds and Precipitation*. Springer Dordrecht.
QUETZERI-SANTIAGO, M.A., CASTREJÓN-PITA, J.R. & CASTREJÓN-PITA, A.A. 2020 On the analysis of the contact angle for impacting droplets using a polynomial fitting approach. *Exp. Fluids* **61** (6), 143.
DE REUCK, A.V.S. 1957 The surface free energy of ice. *Nature* **179** (4570), 1119–1120.
SARLIN, W., GRIVET, R., XU, J., HUERRE, A., SÉON, T. & JOSSERAND, C. 2024 Role of melting and solidification in the spreading of an impacting water drop. *J. Fluid Mech.* **996**, A14.
SAZAKI, G., ZEPEDA, S., NAKATSUBO, S., YOKOMINE, M. & FURUKAWA, Y. 2012 Quasi-liquid layers on ice crystal surfaces are made up of two different phases. *Proc. Natl Acad. Sci. USA* **109** (4), 1052–1055.
SCHOHL, G.A. & ETTEMA, R. 1990 Two-dimensional spreading and thickening of aufeis. *J. Glaciol.* **36** (123), 169–178.
SEBILLEAU, J., ABLONET, E., TORDJEMAN, P. & LEGENDRE, D. 2021 Air humidity effects on water-drop icing. *Phys. Rev. E* **104**, L032802.
SLATER, B. & MICHAELIDES, A. 2019 Surface premelting of water ice. *Nat. Rev. Chem.* **3** (3), 172–188.
TANNER, L.H. 1979 The spreading of silicone oil drops on horizontal surfaces. *J. Phys. D: Appl. Phys.* **12** (9), 1473.
THIÉVENAZ, V., JOSSERAND, C. & SÉON, T. 2020 Retraction and freezing of a water film on ice. *Phys. Rev. Fluids* **5**, 041601.
THIÉVENAZ, V., SÉON, T. & JOSSERAND, C. 2019 Solidification dynamics of an impacted drop. *J. Fluid Mech.* **874**, 756–773.
VAN OSS, C.J., GIESE, R.F., WENTZEK, R., NORRIS, J. & CHUVILIN, E.M. 1992 Surface tension parameters of ice obtained from contact angle data and from positive and negative particle adhesion to advancing freezing fronts. *J. Adhes. Sci. Technol.* **6** (4), 503–516.
VAN DE VELDE, P., FABRE-PARRAS, N., JOSSERAND, C., DUPRAT, C. & PROTIÈRE, S. 2023 Spreading and absorption of a drop on a swelling surface. *Europhys. Lett.* **144** (3), 33001.
VOINOV, O.V. 1976 Hydrodynamics of wetting. *Fluid Dyn.* **11** (5), 714–721.
WANG, Z. 2017 Recent progress on ultrasonic de-icing technique used for wind power generation, high-voltage transmission line and aircraft. *Energy Build.* **140**, 42–49.
WETTLAUFER, J.S. & WORSTER, M.G. 2006 Premelting dynamics. *Annu. Rev. Fluid Mech.* **38** (2006), 427–452.
WINKELS, K.G., WEIJS, J.H., EDDI, A. & SNOEIJER, J.H. 2012 Initial spreading of low-viscosity drops on partially wetting surfaces. *Phys. Rev. E* **85**, 055301.